

Received January 1, 2021, accepted January 14, 2021, date of publication January 18, 2021, date of current version January 27, 2021.

Digital Object Identifier 10.1109/ACCESS.2021.3052469

# 3D Remote Healthcare for Noisy CT Images in the Internet of Things Using Edge Computing

JING ZHANG<sup>1,2</sup>, DAN LI<sup>1</sup>, QIAOZHI HUA<sup>3</sup>, XIN QI<sup>4</sup>,  
ZHENG WEN<sup>5</sup>, AND SAN HLAING MYINT<sup>4</sup>

<sup>1</sup>Department of Computer Science and Technology, Xi'an University of Science and Technology, Xi'an 710054, China

<sup>2</sup>Department of Information Science and Technology, Northwest University, Xi'an 710127, China

<sup>3</sup>Computer School, Hubei University of Arts and Science, Xiangyang 441000, China

<sup>4</sup>Global Information and Telecommunication Institute, Waseda University, Tokyo 169-8050, Japan

<sup>5</sup>School of Fundamental Science and Engineering, Waseda University, Tokyo 169-8050, Japan

Corresponding author: Qiaozhi Hua (11722@hbuas.edu.cn)

This work was supported in part by the National Natural Science Foundation of China under Grant 61902311, in part by the Postdoctoral Research Foundation of China under Grant 2019M663801, in part by the Scientific Research Plan of Shaanxi Provincial Education Department under Grant 19JK0541, and in part by the Counterpart Service for the Construction of Xiangyang Science and Technology Innovation China Innovative Pilot City.

**ABSTRACT** Edge computing can provide many key functions without connecting to centralized servers, which enables remote areas to obtain real-time medical diagnoses. The combination of edge computing and Internet of things (IoT) devices can send remote patient data to the hospital, which will help to more effectively address long-term or chronic diseases. CT images are widely used in the diagnosis of clinical diseases, and their characteristics are an important basis for pathological diagnosis. In the CT imaging process, speckle noise is caused by the interference of ultrasound on human tissues, and its component information is complex. To solve these problems, we propose a 3D reconstruction method for noisy CT images in the IoT using edge computing. First, we propose a multi-stage feature extraction generative adversarial network (MF-GAN) denoising algorithm. The generator of MF-GAN adopts the multi-stage feature extraction, which can ensure the reconstruction of the image texture and edges. Second, we apply the denoised images generated from the MF-GAN method to perform the 3D reconstruction. A marching cube (MC) algorithm based on regional growth and trilinear interpolation (RGT-MC) is proposed. With the idea of regional growth, all voxels containing iso-surfaces are selected and calculated, which accelerates the reconstruction efficiency. The intersection point of the voxel and iso-surface is calculated by the trilinear interpolation algorithm, which effectively improves the reconstruction accuracy. The experimental results show that MF-GAN has a better denoising effect than other algorithms. Compared to other representative 3D algorithms, the RGT-MC algorithm greatly improves the efficiency and precision.

**INDEX TERMS** Internet of Things, edge computing, generative adversarial network, 3D reconstruction.

## I. INTRODUCTION

In the past decade, Internet of Things (IoT) medical devices have become increasingly common, such as wearable sensors and blood glucose monitors [1]. The combination of edge computing and IoT devices can send remote patient data to the hospital in real time, which will help more effectively address long-term or chronic diseases [2]. Edge computing can help hospitals establish a remote medical network, which can provide online and real-time doctor services for patients in any place.

The associate editor coordinating the review of this manuscript and approving it for publication was Zhenyu Zhou.

With the increasing amount of patient diagnosis data in the medical industry, edge computing will reduce the amount of moving data and improve the efficiency [3]. Using the edge computing infrastructure, doctors can obtain the data directly without going through remote centralized servers. The edge computing infrastructure reduces the dependence on remote centralized servers [4], which implies that doctors will obtain a more flexible and faster network to diagnose patients.

However, speckle noise in CT images causes severe visual interference and obscures the image's features [5]. Speckle noise is caused by the interference of ultrasound on human tissues, and its component information is complex. In addition, CT images cannot provide the 3D shape of organs, which seriously affects the doctor's diagnosis.

Therefore, it is necessary to combine CT image denoising technology [6] with a 3D reconstruction algorithm [7] to provide a more reliable basis for clinical diagnosis and operation planning.

Deep learning methods have rapidly developed in IoT [8], and many researchers have begun to design a deep learning structure for image denoising. Jain *et al.* [9] first used CNN for denoising algorithms and proved that convolutional neural networks could directly learn nonlinear mapping from low-quality images to clean images. Chen and Pock [10] proposed the trainable nonlinear reaction diffusion (TNRD) method, which verified that the performance of the model was greatly improved with an increase in number of layers. Mao *et al.* [11] proposed automatic deep convolutional coding for image restoration, which proved to have a better denoising effect. Zhang *et al.* [12] first introduced residual learning and batch standardization into image denoising and proposed a denoising convolution neural network (DnCNN), although these methods can effectively improve the effect of noise removal. However, these methods did not give more consideration to the problems of image detail smoothing and edge information loss. To solve these problems, we propose a multi-stage feature extraction generative adversarial network (MF-GAN) denoising algorithm for CT images. The generator of MF-GAN adopts multi-stage feature extraction, which can ensure the reconstruction of image texture and edges.

For the 3D reconstruction of CT images, the marching cube (MC) algorithm is a typical high-quality 3D reconstruction method [13]. Masala's algorithm [14] replaced 15 basic topological configurations with 21 configurations, which improved the accuracy of 3D reconstruction of images. Shuai's algorithm [15] simplified the operation process of MC and improved the efficiency of the algorithm by selecting the golden section point. This paper proposes the MC algorithm based on the regional growth and trilinear interpolation (RGT-MC) 3D reconstruction algorithm. With the idea of regional growth [16], all voxels containing iso-surfaces are selected and calculated, which accelerates the reconstruction efficiency. The intersection point of the voxel and iso-surface is calculated by the trilinear interpolation algorithm [17], which effectively improves the reconstruction accuracy.

The contributions of this paper are listed as follows:

a) We create a 3D reconstruction method for denoised images in the IoT using the edge computing infrastructure. Patients can provide CT images at any place for rapid and effective diagnosis, which enables remote areas to obtain real-time medical diagnosis.

b) We create a MF-GAN denoising algorithm. The generator of MF-GAN adopts multi-stage feature extraction, including multi-scale feature extraction and high-level feature extraction, which can ensure the reconstruction of the image texture and edges.

c) We create a RGT-MC method for the 3D reconstruction. With the idea of regional growth, all voxels containing iso-surfaces are selected and calculated, which accelerates the reconstruction efficiency. The intersection point of the

voxel and iso-surface is calculated by the trilinear interpolation algorithm, which effectively improves the reconstruction accuracy.

## II. OUR APPROACH

### A. MF-GAN DENOISING ALGORITHM OF CT IMAGES

CT images are widely used in the diagnosis of clinical diseases in IoT [18]. Speckle noise in CT images causes severe visual interference and obscures the image's feature information. To solve this problem, this paper proposes a MF-GAN denoising algorithm, which uses the generator of multi-stage feature extraction to ensure the reconstruction of image texture and edges.

#### 1) SPECKLE NOISE OF CT IMAGES

When ultrasound travels through the human body, it will emit, scatter, refract, diffract and interfere with different tissue interfaces [19]. The interference is the direct cause of speckle noise. The speckle noise intensity is smaller when the interference is cancellative and larger when the interference is phase length.

The distribution of speckle noise in CT images is complex. Most researchers think that speckle noise is a Rayleigh distribution [20] under ideal conditions. The Rayleigh distribution expression is shown in formula (1), and its probability density is shown in formula (2).

$$F(x) = 1 - \exp\left(-\frac{x^2}{2\sigma^2}\right), \quad x > 0, \sigma > 0 \quad (1)$$

$$f(x) = \frac{x}{\sigma^2} \exp\left(-\frac{x^2}{2\sigma^2}\right), \quad x > 0, \sigma > 0 \quad (2)$$

where  $\sigma$  is related to the mean of the speckle intensity.

Some researchers also believe that speckle noise is a gamma distribution [21] in practice. The gamma distribution is a continuous probability function in statistics.

$$f(x, \alpha, \beta) = \begin{cases} \frac{\beta^\alpha x^{\alpha-1}}{\Gamma(\alpha)} \exp(-\beta x), & x \geq 0 \\ 0, & x < 0 \end{cases} \quad (3)$$

where random variable  $x$  obeys the gamma distribution and is counted as  $x \sim \Gamma(\alpha, \beta)$ .

The speckle noise information is complex, including multiplicative and additive noise [22]. Formula (4) is constructed to represent speckle noise, where  $f(x, y)$  is a CT image with speckle noise,  $g(x, y)$  is a real image without speckle noise,  $n_1(x, y)$  is a multiplicative noise part, and  $n_2(x, y)$  is an additive noise part. Many researchers have found that the multiplicative part of speckle noise has a much greater impact than the additive part.

$$f(x, y) = g(x, y) * n_1(x, y) + n_2(x, y) \quad (4)$$

$$f(x, y) = g(x, y) * n(x, y) \quad (5)$$

#### 2) NETWORK ARCHITECTURE OF MF-GAN

Generator  $G$  of MF-GAN is a denoising network, whose input is a noisy image and whose output is a denoised image. The input of discriminator  $D$  is a denoised image and sharp image,

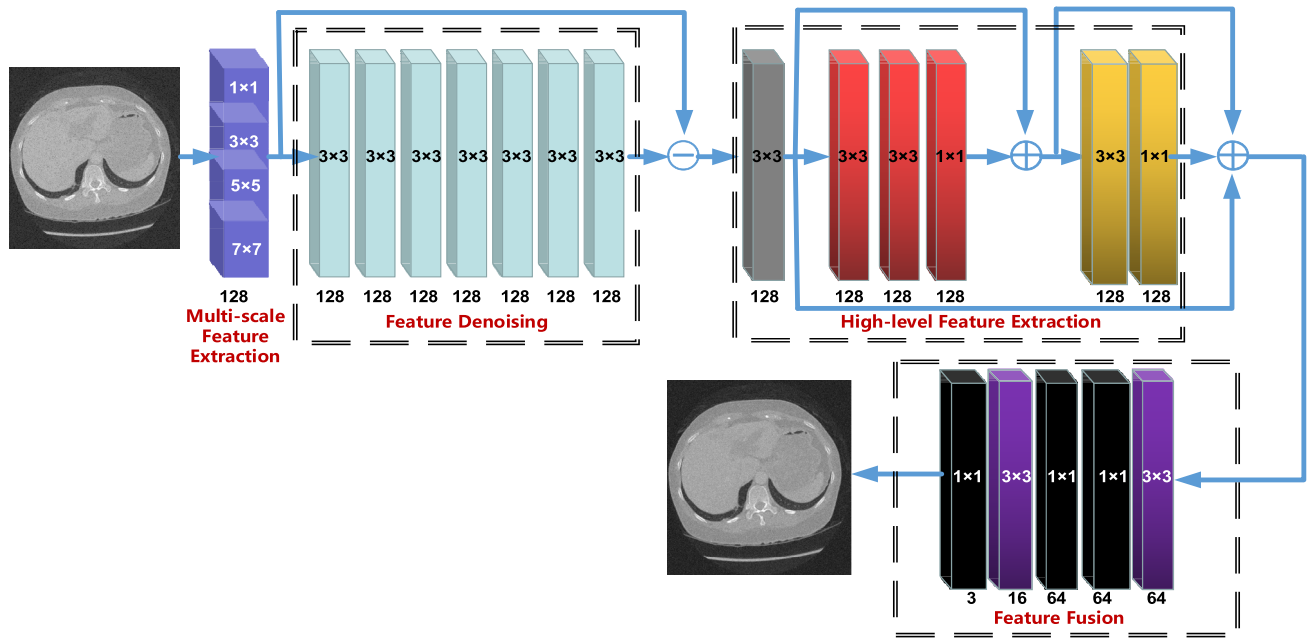


FIGURE 1. Overall structure of MF-GAN generator.

and the output value is 0-1, which represents the similarity between denoised image and sharp image [23].

When the generator  $G$  is optimized, the parameters of the discriminator  $D$  are kept constant. Set  $V(G)$  as the minimum value and  $D(G(z))$  close to 1, which makes the discriminator unable to distinguish the real image from the denoised image [24]. When the discriminator  $D$  is optimized, the parameters of the generator  $G$  are kept constant. Set  $V(D)$  as the maximum value,  $D(x)$  close to 1, and  $D(G(z))$  close to 0, which improves the performance of the discriminator. Through training of MF-GAN, the optimal solution is obtained for generator  $G$  and discriminator  $D$ .

$$V(D, G) = E_{x \sim P_{data(x)}} [\log D(x)] + E_{z \sim P_{z(z)}} [\log(1 - D(G(z)))] \quad (6)$$

When the discriminator  $D$  is optimal, the parameters of the generator  $G$  in formula (6) remain constant, Then

$$V(D) = \int_x [p_r(x) \log D(x) + p_g(x) \log(1 - D(x))] dx \quad (7)$$

where  $p_r$  represents the real image, and  $p_g$  represents the result of the generator  $G(z)$ . When  $V(D)$  takes the maximum value, the  $D(x)$  value is obtained as shown:

$$D(x) = \frac{p_r(x)}{p_r(x) + p_g(x)} \quad (8)$$

The loss function  $V(G)$  of the generator is expressed as:

$$V(G) = E_{x \sim p_r} [\log D(x)] + E_{x \sim p_g} [\log(1 - D(x))] \quad (9)$$

## ① GENERATOR

The overall structure of the generator  $G$  is shown in Figure 1. The generator of MF-GAN is divided into four stages: multi-scale feature extraction; feature denoising; high-level

feature extraction; and feature fusion. To avoid losing more image details, our generator adopts multi-stage feature extraction.

### a: MULTI-SCALE FEATURE EXTRACTION

The feature extraction layer consists of convolution kernels with different sizes:  $1 \times 1$ ,  $3 \times 3$ ,  $5 \times 5$ , and  $7 \times 7$ . For convolution kernels of different sizes, which correspond to different size perception fields in the input image, the  $1 \times 1$  convolution kernel retains high-frequency information, and the  $7 \times 7$  convolution kernel can extract sufficient useful features. The image structure can be fully extracted by a large-scale convolution kernel [25], and the detailed information can be saved by a small-scale convolution kernel. The multi-scale features provide sufficient information for the high-level feature extraction and fusion, which can restore the image texture and edges.

The number of output channels of each convolution kernel is set to 32, and all output channels are combined according to the dimension. Therefore, 128 output channels are obtained for the four convolution kernels. The image boundaries are filled with zeros to keep the input and output dimensions consistent [26].

### b: FEATURE DENOISING

The denoised features are obtained by subtracting the noisy features and extracted noises through the cross-layer connection.

In Figure 1, a seven-layer stacked convolution layer is used to extract noisy features. Each layer of the convolution network uses a  $3 \times 3$  convolution kernel. We take ReLU as the activation function. A cross-layer connection structure is used between the original multi-scale features and the extracted noisy features, which subtracts the multi-scale features from the extracted noise distribution.

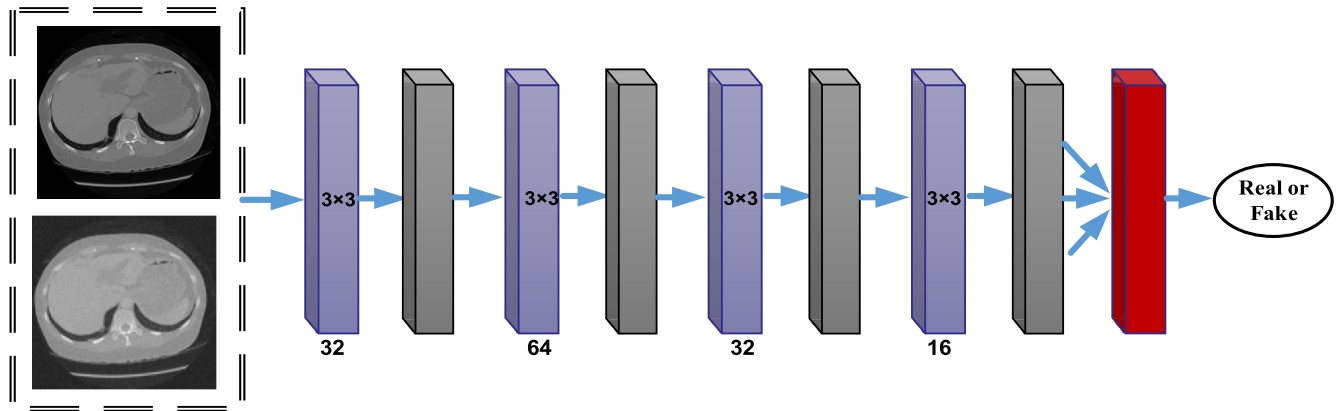


FIGURE 2. Overall structure of MF-GAN discriminator.

### c: HIGH-LEVEL FEATURE EXTRACTION

First, a layer of a  $3 \times 3$  convolution network is used to fuse the denoised features, which is represented by a grey box in Figure 1. Second, a stack residual network is used to extract and fuse the high-level features. In the stack residual network [27], the first part adopts two layers of  $3 \times 3$  to extract large-scale features and a  $1 \times 1$  convolution kernel to fuse the features. The second part uses a layer of  $3 \times 3$  to extract small-scale features and a  $1 \times 1$  convolution kernel to fuse the features.

### d: FEATURE FUSION

After obtaining the high-level features of the image, the features must be further filtered and fused to reconstruct the denoised images. Two layers of  $3 \times 3$  convolution kernel and three layers of  $1 \times 1$  convolution kernel are used to filter and fuse the features. The multi-layer network is used to filter the features, which have more noise or less information.

The filtered features are gradually fused, and a correct denoised image is constructed by using the nonlinearity of the multi-layer network.

## ② DISCRIMINATOR

The discriminator  $D$  of MF-GAN uses four convolution layers to extract image features, as shown in Figure 2. Each convolution layer is processed by batch normalization [28]. The  $3 \times 3$  convolution kernel is used to extract and fuse the texture features of the image. The number of output channels of the convolution layers are 32, 64, 32, and 16. In Figure 2, the down-sampling layer is represented by black boxes. The down-sampling factor is 2, which implies that each down-sampling changes the length and width of the feature to half. The maximum pooling is selected for the down sampling operation to retain more texture features and reduce the number of parameters [29].

In Figure 2, at the output of the four convolution, a fully connected layer is added to weight the extracted features, which is represented by a red box. The output value represents the probability that the input image is a sharp image. In the last layer, the sigmoid activation function is used to limit the output value between 0 and 1.

## B. RGT-MC 3D RECONSTRUCTION ALGORITHM

In this paper, the marching cube (MC) algorithm [30] based on regional growth and trilinear interpolation (RGT-MC) is proposed. First, with the idea of regional growth, all voxels that contain an iso-surface are selected and calculated, which accelerates the reconstruction efficiency. Second, the intersection point of the voxel and iso-surface is calculated by the trilinear interpolation algorithm, and the intersection point is calculated by the gray value of eight voxel vertices, which effectively improves the reconstruction accuracy.

The RGT-MC algorithm includes five steps as follows:

*Step 1:* Select the seed voxel. For two CT images, a voxel is created from four adjacent pixels on one CT image and four adjacent pixels on the next CT image, as shown in Figure 3. One seed voxel is randomly selected.

*Step 2:* Extract voxels that contain an iso-surface using the regional growth method. The regional growth method is used to address six neighborhoods of seed voxels to form a region and determine whether the region contains an iso-surface. If yes, skip step 3; If no, skip step 1.

*Step 3:* Determine the subdivision method of the iso-surface. We use the traditional MC algorithm to determine the subdivision of the iso-surface, which includes 15 basic subdivisions.

*Step 4:* Calculate the intersection of the iso-surface and voxel by the trilinear interpolation algorithm. The trilinear interpolation method is used to calculate the coordinates of each intersection point. According to the index of the vertex and edge of the voxel, the edge of the voxel that intersects with the iso-surface is found.

*Step 5:* Determine whether to traverse all voxels containing iso-surfaces. If yes, the algorithm is completed; if no, skip step 1.

### 1) REGIONAL GROWTH ALGORITHM

The basic idea of the regional growth algorithm is to combine similar voxels to form a region. In the improved algorithm, the problem is how to determine whether the adjacent voxels contain iso-surfaces, and each voxel contains 8 vertices and 6 faces [31]. In Figure 4, four voxels are adjacent, and AB is the common edge. The two lower voxels are adjacent to each



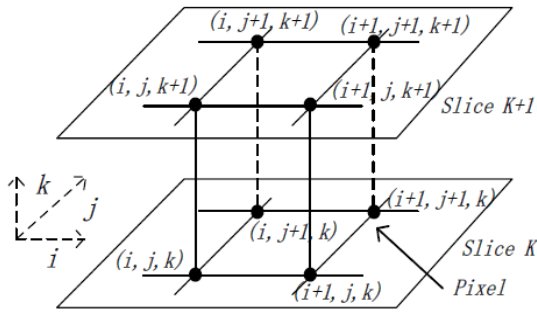


FIGURE 3. Diagram of a voxel.

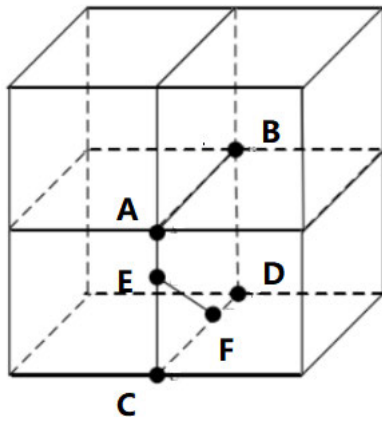


FIGURE 4. Diagram of four adjacent voxels.

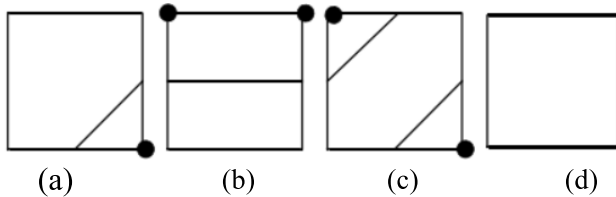


FIGURE 5. States of the four vertices on the surface.

other and have a common face ABCD. If these four vertices A, B, C, and D are not simultaneously greater than or less than the set threshold, there are iso-surfaces in the adjacent voxels. In Figure 4, EF is the intersection line between the iso-surface and the voxel at the lower left. However, the intersection line EF also exists in the adjacent voxels at the lower right, so the lower right voxel also contains the iso-surface.

To determine whether the voxels adjacent to the seed voxels contain the iso-surface, it is only necessary to consider the states of four vertices on the surface. For the states of the four vertices on the surface, there are four cases, as shown in Figure 5: (a) one vertex is different from other states; (b), (c) two vertices are different from other states; (d) all vertices have the same state. In summary, the four vertices are in one of three states (a), (b) and (c), and the adjacent voxel contains an iso-surface.

## 2) TRILINEAR INTERPOLATION ALGORITHM

For any point  $(x, y, z)$  in a voxel, the trilinear interpolation method linearly calculates the value of point  $(x, y, z)$  through

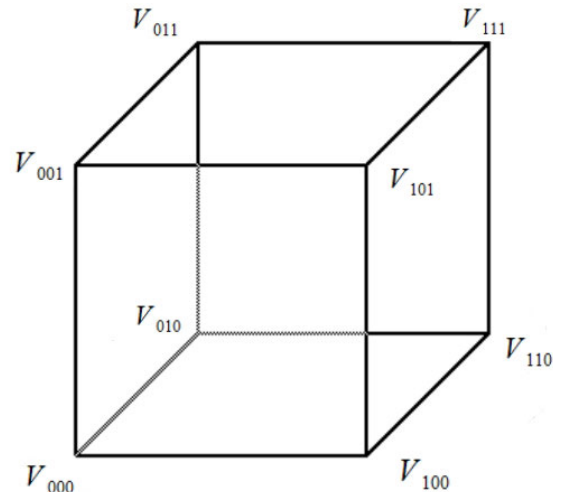


FIGURE 6. Values of each vertex of a voxel.

eight vertices on the voxel [32]. As shown in Figure 6, the value of each vertex of a voxel is expressed as  $V_{000}, V_{100}, V_{010}, \dots, V_{111}$ .

The point  $V_{xyz}$  in the voxel is expressed as:

$$\begin{aligned} V_{xyz} = & V_{000}(1-x)(1-y)(1-z) + V_{100}x(1-y)(1-z) \\ & + V_{010}(1-x)y(1-z) + V_{001}(1-x)(1-y)z \\ & + V_{101}x(1-y)z + V_{011}(1-x)y z \\ & + V_{110}xy(1-z) + V_{111}xyz \end{aligned} \quad (10)$$

By introducing the gray values of the eight vertices and iso-surfaces into formula (10), we obtain the intersection point of the iso-surface and voxel on this edge.

## III. EXPERIMENTS

The combination of edge computing and IoT devices can send remote patient data to the hospital in real time, which will help to more effectively address long-term or chronic diseases. For performance evaluation of denoised CT images, we selected 2000 CT images of the liver from the 3D-IRCADb-01 database [33] (<https://www.ircad.fr/research/3d-ircadb-01/>). The 3D-IRCADb-01 database is composed of 3D CT scans of 10 women and 10 men with liver tumors in 75% of cases.

### A. EXPERIMENT OF MF-GAN DENOISING ALGORITHM

We consider the diagnosis results of two liver tumor patients as examples. Figure 7 shows two CT images of a 64-year-old male with liver cancer. Figure 8 shows two CT images of a 74-year-old female with liver cancer.

#### 1) GENERATION OF SPECKLE NOISY IMAGES

Speckle noise in CT images is similar to multiplicative noise. Our MF-GAN denoising algorithm adopts Rayleigh and Gamma distribution multiplicative noise.

##### a: RAYLEIGH DISTRIBUTION

In Figure 9 and Figure 10, (a) shows the original CT image. (b) shows the corresponding noisy CT images with Rayleigh distribution multiplicative noise.

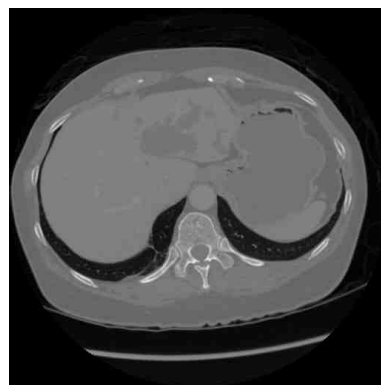


**FIGURE 7.** CT images of 64 years old male with liver cancer.

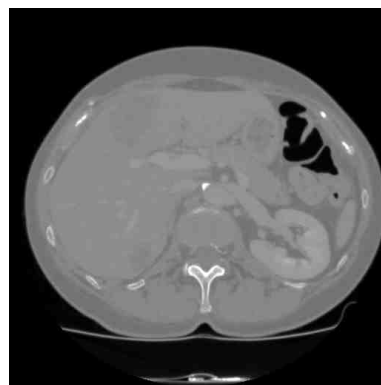
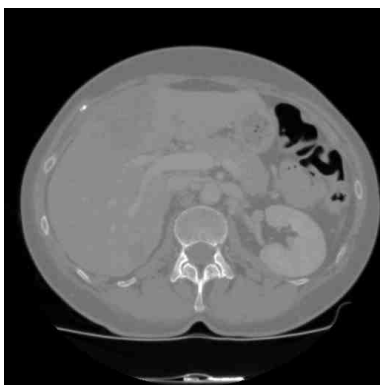


**FIGURE 8.** CT images of 74 years old female with liver cancer.



(a) Original CT image



(b) Noisy CT images

**FIGURE 9.** Noisy CT images with Rayleigh distribution of 64 years old male with liver cancer.

#### *b: GAMMA DISTRIBUTION*

In Figure 11 and Figure 12, (a) shows the original CT image. (b) shows the corresponding noisy CT images with Gamma distribution multiplicative noise.

### 2) PERFORMANCE OF MF-GAN

#### *a: QUALITATIVE EVALUATION*

To verify the effectiveness of the MF-GAN denoising algorithm, the same CT image is denoised by five different methods. For different classic algorithms, our algorithm is compared with Jain's algorithm [9], Chen's algorithm [10], Mao's algorithm [11] and Zhang's algorithm [12].

In Figure 13 and Figure 14, Jain's algorithm shows that the edge is slightly visible compared to the original image. Chen's algorithm and Mao's algorithm show that the details of the reconstructed image are obviously fuzzy. Zhang's algorithm would get better denoised results, but these methods do not give more consideration to the problems of image detail smoothing and edge information loss. Our MF-GAN adopts the multi-stage feature extraction generator, which can restore the image texture and edge.

#### *b: QUANTITATIVE EVALUATION*

Peak Signal-to-Noise Ratio (PSNR) [34] and Structural Similarity (SSIM) [35] are used as evaluation indicators.

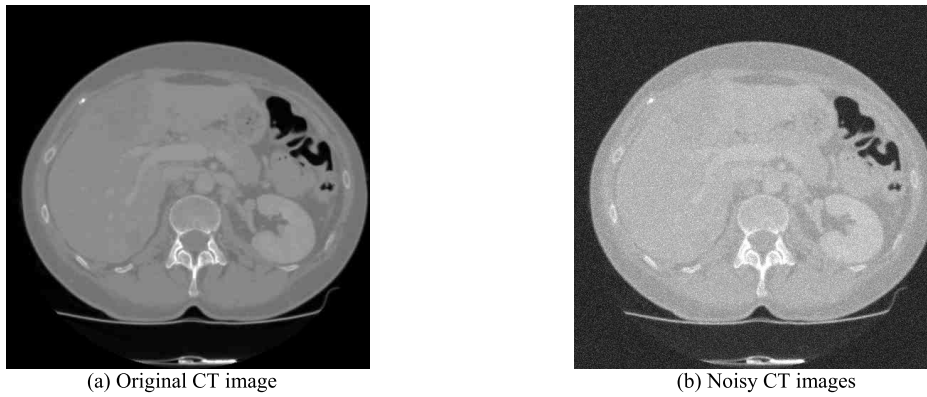


**FIGURE 10.** Noisy CT images with Rayleigh distribution of 74 years old female with liver cancer.

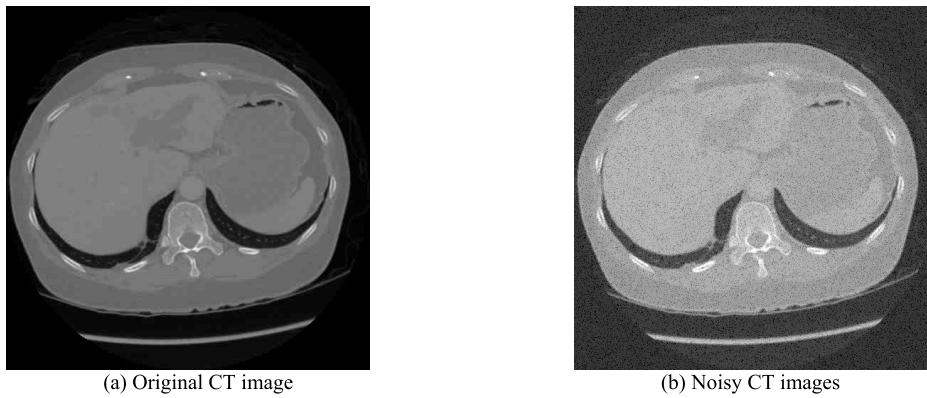


**FIGURE 11.** Noisy CT images with Gamma distribution of 64 years old male with liver cancer.

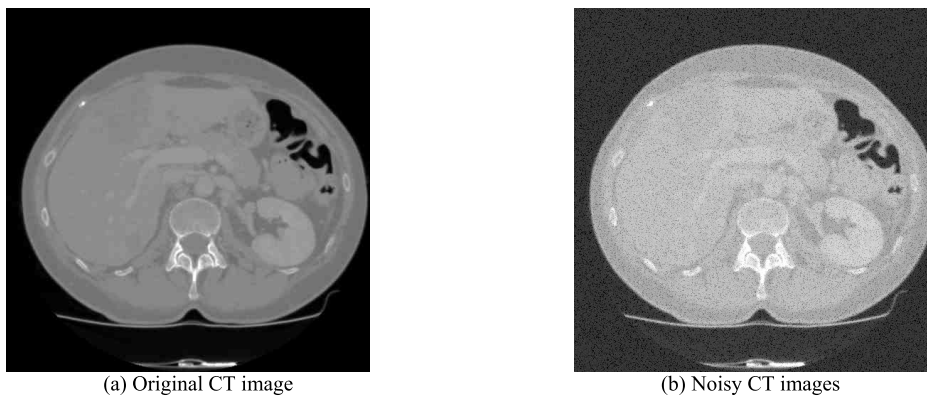


**FIGURE 12.** Noisy CT images with Gamma distribution of 74 years old female with liver cancer.

Table 1 shows the denoised results of various algorithms for a 64-year-old male with liver cancer, which adopts noisy CT images with a Rayleigh distribution. Table 2 shows the denoised results of various algorithms for 74-year-old females with liver cancer, which adopts noisy CT images with a gamma distribution. It can be seen that the PSNR value of our MF-GAN algorithm is greater than the other four representative algorithms. The SSIM value of our MF-GAN algorithm is close to 1, which achieves a better reconstruction effect.

### B. 3D RECONSTRUCTION EXPERIMENT

The CT image size is  $512 \times 512$  pixels. The first liver cancer patient had 200 CT images for 3D reconstruction and

was a 64-year-old male. The second liver cancer patient had 129 CT images for 3D reconstruction and was a 74-year-old female. Therefore, the dimensions of the two data sets are  $512 \times 512 \times 199$  and  $512 \times 512 \times 128$ .

#### 1) PERFORMANCE OF 3D RECONSTRUCTION

In Table 3, the Masala's algorithm [14] replaces 15 basic topological configurations with 21 configurations, which produces a very large time cost. The Shuai's algorithm [15] and RGT-MC algorithm greatly improves the efficiency of 3D reconstruction.

#### 2) ACCURACY OF 3D RECONSTRUCTION

The accuracy of 3D reconstruction is the proportion of the 3D area to the real liver area. The results of the 3D



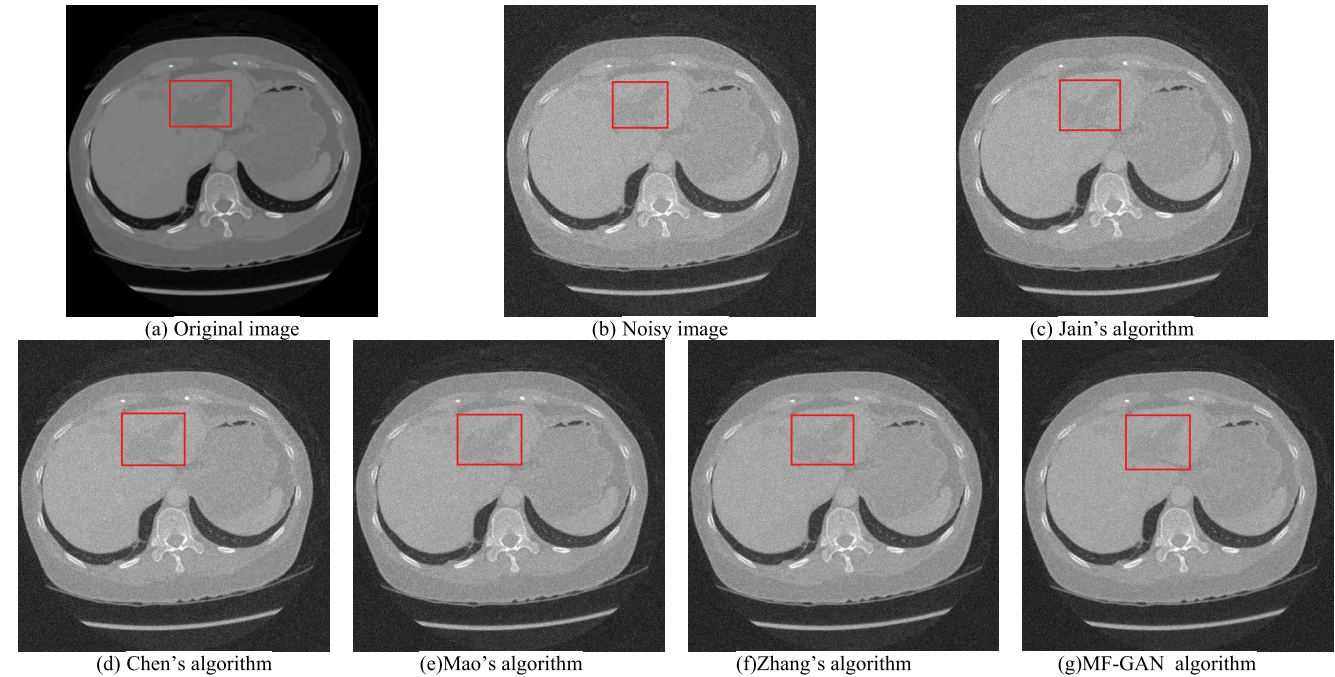


FIGURE 13. Denoised images of various algorithms for 64 years old male with liver cancer with a Rayleigh distribution.

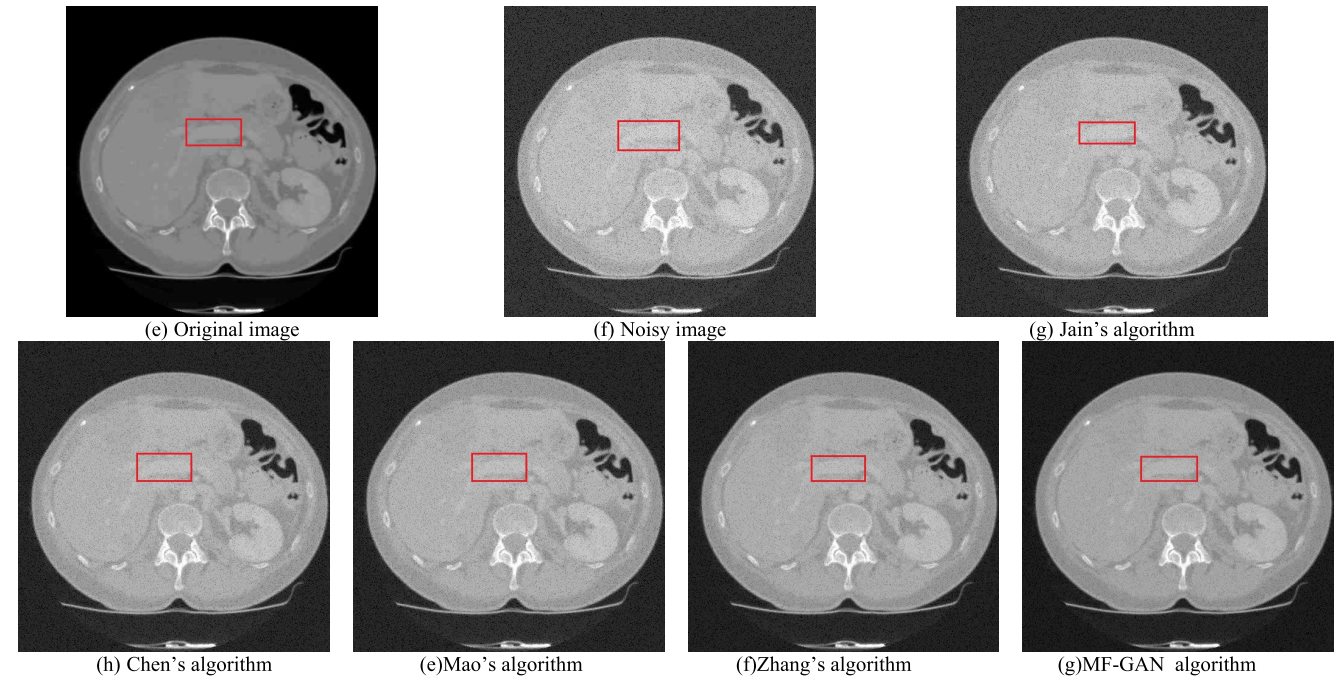


FIGURE 14. Denoised images of various algorithms for 74 years old female with liver cancer with a Gamma distribution.

TABLE 1. The denoised results of various algorithms for 64 years old male with liver cancer.

Similarity Indicator	Comparison Algorithm				
	Jain's algorithm	Chen's algorithm	Mao's algorithm	Zhang's algorithm	MF-GAN algorithm
PSNR	25.1036	27.7577	27.9381	28.5594	29.3569
SSIM	0.7466	0.7601	0.7864	0.8314	0.8514

reconstruction are compared to those of the doctor's manual label.

The spatial iso-surface display generated by the traditional MC algorithm is not sufficiently smooth. Shuai's

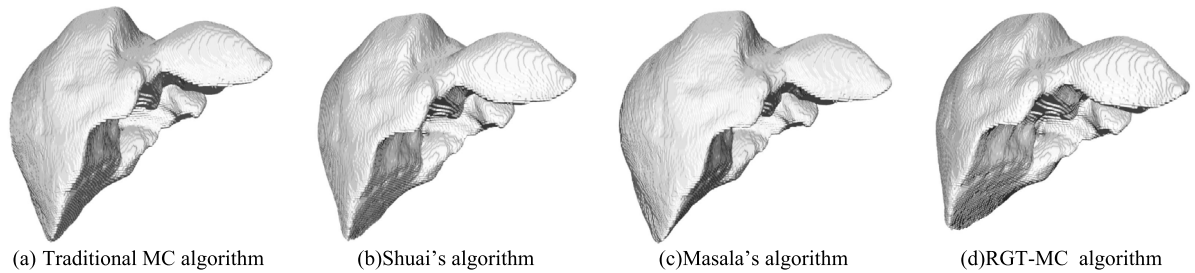
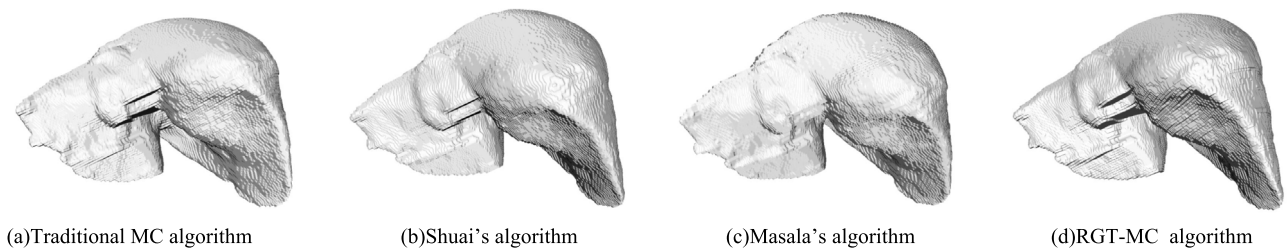


**TABLE 2.** The denoised results of various algorithms for 74 years old female with liver cancer.

Similarity Indicator	Comparison Algorithm				
	Jain's algorithm	Chen's algorithm	Mao's algorithm	Zhang's algorithm	MF-GAN algorithm
PSNR	25.7653	27.6223	27.8614	28.4921	29.0979
SSIM	0.7347	0.7588	0.7721	0.8256	0.8656

**TABLE 3.** Comparison results of 3D reconstruction performance.

Data Set	Data Dimension	Algorithm Name	Time Cost (ms)
64 years old male liver cancer patient	$512 \times 512 \times 199$	Traditional MC algorithm	12817
		Masala's algorithm	14361
		Shuai's algorithm	874
		RGT-MC algorithm	553
74 years old female liver cancer patient	$512 \times 512 \times 128$	Traditional MC algorithm	8341
		Masala's algorithm	9263
		Shuai's algorithm	567
		RGT-MC algorithm	358

**FIGURE 15.** 3D reconstruction results of various algorithms for 64 years old male with liver cancer.**FIGURE 16.** 3D reconstruction results of various algorithms for 74 years old female with liver cancer.**TABLE 4.** Comparison results of 3D reconstruction accuracy for 64 years old male with liver cancer.

Algorithm Name	Traditional MC algorithm	Shuai's algorithm	Masala's algorithm	RGT-MC algorithm
3D reconstruction accuracy	76.2%	77.3%	86.5%	90.7%

algorithm does not improve the reconstruction accuracy compared to the traditional MC algorithm. The reconstruction result of Masala's algorithm is smooth because of the extended topology. The RGT-MC algorithm uses trilinear interpolation to calculate the intersection of the iso-surface

and voxel, which improves the smoothness of the 3D reconstruction surface.

In Table 4 and Table 5, for the 64 years old male liver cancer patient, the reconstruction accuracy of RGT-MC algorithm is improved by 14.5%, 13.4% and 4.2% respectively.

**TABLE 5. Comparison results of 3D reconstruction accuracy for 74 years old female with liver cancer.**

Algorithm Name	Traditional MC algorithm	Shuai's algorithm	Masala's algorithm	RGT-MC algorithm
3D reconstruction accuracy	78.5%	79.6%	88.5%	91.2%

For the 74 years old female liver cancer patient, the reconstruction accuracy of RGT-MC algorithm is improved by 12.7%, 11.6% and 2.7% respectively.

#### IV. CONCLUSION

In this paper, a 3D reconstruction method for noisy CT images in the IoT using edge computing is proposed. First, we propose a MF-GAN denoising algorithm. The generator of MF-GAN adopts multi-stage feature extraction, including multi-scale feature extraction and high-level feature extraction, which can ensure the reconstruction of image texture and edges. Second, we propose a RGT-MC algorithm. With the idea of regional growth, all voxels containing the iso-surface are selected and calculated, which accelerates the reconstruction efficiency. The intersection point of the voxel and iso-surface is calculated by the trilinear interpolation algorithm, which effectively improves the reconstruction accuracy.

Using the edge computing infrastructure, doctors can directly obtain the data without going through remote centralized servers [36], [37]. Patients can wear IoT medical devices at any place for rapid and effective diagnosis. With the increasing number of IoT devices, it brings extra burden to the network infrastructure, which makes edge computing widely used in medical IoT scenarios. On one hand, through IoT devices and edge computing infrastructure, we can expand the coverage of the existing network, enabling doctors to treat patients in areas with poor connectivity. On the other hand, edge computing saves costs in the whole medical process, such as the doctors' remote diagnosis, medical equipment and supplies.

#### ACKNOWLEDGMENT

Jing Zhang and Dan Li are co-first authors.

#### REFERENCES

- [1] Z. Guo, Y. Shen, A. K. Bashir, M. Imran, N. Kumar, D. Zhang, and K. Yu, "Robust spammer detection using collaborative neural network in Internet of Thing applications," *IEEE Internet Things J.*, early access, Jun. 19, 2020, doi: [10.1109/JIOT.2020.3003802](https://doi.org/10.1109/JIOT.2020.3003802).
- [2] X. Zhang, L. Yang, Z. Ding, J. Song, Y. Zhai, and D. Zhang, "Sparse vector coding-based multi-carrier NOMA for in-home health networks," *IEEE J. Sel. Areas Commun.*, vol. 32, no. 2, pp. 325–337, Feb. 2021, doi: [10.1109/JSAC.2020.3020679](https://doi.org/10.1109/JSAC.2020.3020679).
- [3] Z. Zhou, H. Liao, B. Gu, K. M. S. Huq, S. Mumtaz, and J. Rodriguez, "Robust mobile crowd sensing: When deep learning meets edge computing," *IEEE Netw.*, vol. 32, no. 4, pp. 54–60, Jul. 2018, doi: [10.1109/MNET.2018.1700442](https://doi.org/10.1109/MNET.2018.1700442).
- [4] K.-P. Yu, L. Tan, M. Aloqaily, H. Yang, and Y. Jararweh, "Blockchain-enhanced data sharing with traceable and direct revocation in IIoT," *IEEE Trans. Ind. Informat.*, early access, Jan. 5, 2021, doi: [10.1109/TII.2021.3049141](https://doi.org/10.1109/TII.2021.3049141).
- [5] J. H. Lin, S. C. Chang, Y. H. Li, C. Y. Chien, C. H. Chen, Y. C. Lin, J. J. Wu, S. Y. Tsay, Y. H. Chen, "Investigation of laser speckle noise suppression by using polymer-stabilized liquid crystals within twisted nematic cell," *Appl. Phys. Exp.*, vol. 10, no. 3, pp. 1–4, 2017, doi: [10.7567/APEX.10.031701](https://doi.org/10.7567/APEX.10.031701).
- [6] Q. Yang, P. Yan, Y. Zhang, H. Yu, Y. Shi, X. Mou, M. K. Kalra, Y. Zhang, L. Sun, and G. Wang, "Low-dose CT image denoising using a generative adversarial network with wasserstein distance and perceptual loss," *IEEE Trans. Med. Imag.*, vol. 37, no. 6, pp. 1348–1357, Jun. 2018, doi: [10.1109/TMI.2018.2827462](https://doi.org/10.1109/TMI.2018.2827462).
- [7] X. Zheng, S. Ravishankar, Y. Long, and J. A. Fessler, "PWLS-ULTRA: An efficient clustering and learning-based approach for low-dose 3D CT image reconstruction," *IEEE Trans. Med. Imag.*, vol. 37, no. 6, pp. 1498–1510, Jun. 2018, doi: [10.1109/TMI.2018.2832007](https://doi.org/10.1109/TMI.2018.2832007).
- [8] K. Yu, L. Lin, M. Alazab, L. Tan, and B. Gu, "Deep learning-based traffic safety solution for a mixture of autonomous and manual vehicles in a 5G-enabled intelligent transportation system," *IEEE Trans. Intell. Transp. Syst.*, early access, Dec. 22, 2020, doi: [10.1109/TITS.2020.3042504](https://doi.org/10.1109/TITS.2020.3042504).
- [9] V. Jain and H. S. Seung, "Natural image denoising with convolutional networks," in *Proc. Int. Conf. Neural Inf. Process. Syst.* Red Hook, NY, USA: Curran Associates, 2008, pp. 769–776.
- [10] Y. Chen and T. Pock, "Trainable nonlinear reaction diffusion: A flexible framework for fast and effective image restoration," *IEEE Trans. Pattern Anal. Mach. Intell.*, vol. 39, no. 6, pp. 1256–1272, Jun. 2017, doi: [10.1109/TPAMI.2016.2596743](https://doi.org/10.1109/TPAMI.2016.2596743).
- [11] X. J. Mao, C. Shen, and Y. B. Yang, "Image denoising using very deep fully convolutional encoder-decoder networks with symmetric skip connections," in *Proc. 30th Int. Conf. Neural Inf. Process. Syst. (NIPS)*, Barcelona, Spain, 2016, pp. 2810–2818.
- [12] K. Zhang, W. Zuo, Y. Chen, D. Meng, and L. Zhang, "Beyond a Gaussian denoiser: Residual learning of deep CNN for image denoising," *IEEE Trans. Image Process.*, vol. 26, no. 7, pp. 3142–3155, Jul. 2017, doi: [10.1109/TIP.2017.2662206](https://doi.org/10.1109/TIP.2017.2662206).
- [13] T. Ding, H. Hu, C. Bai, S. Guo, M. Yang, S. Wang, and M. Wan, "Spatial-temporal three-dimensional ultrasound plane-by-plane active cavitation mapping for high-intensity focused ultrasound in free field and pulsatile flow," *Ultrasonics*, vol. 69, pp. 166–181, Jul. 2016, doi: [10.1016/j.ultras.2016.04.010](https://doi.org/10.1016/j.ultras.2016.04.010).
- [14] G. L. Masala, B. Golosio, and P. Oliva, "An improved marching cube algorithm for 3D data segmentation," *Comput. Phys. Commun.*, vol. 184, no. 3, pp. 777–782, Mar. 2013, doi: [10.1016/j.cpc.2012.09.030](https://doi.org/10.1016/j.cpc.2012.09.030).
- [15] R. J. Shuai and S. J. Chen, "An improved MC three-dimensional reconstruction algorithm," *China Digit. Med.*, vol. 11, no. 3, pp. 83–86, 2016, doi: [10.3969/j.issn.1673-7571.2016.03.028](https://doi.org/10.3969/j.issn.1673-7571.2016.03.028).
- [16] J. E. Solly, N. J. Cuniffe, and C. J. Harrison, "Regional growth rate differences specified by apical notch activities regulate liverwort thallus shape," *Current Biol.*, vol. 27, no. 1, pp. 16–26, Jan. 2017, doi: [10.1016/j.cub.2016.10.056](https://doi.org/10.1016/j.cub.2016.10.056).
- [17] C. Q. T. Thanh and N. T. Hai, "Trilinear interpolation algorithm for reconstruction of 3-D MRI brain image," *Amer. J. Signal Process.*, vol. 7, no. 1, pp. 1–11, 2017, doi: [10.5923/j.ajsp.20170701.01](https://doi.org/10.5923/j.ajsp.20170701.01).
- [18] T. R. Bennett, N. Gans, and R. Jafari, "Data-driven synchronization for Internet-of-Things systems," *ACM Trans. Embedded Comput. Syst.*, vol. 16, no. 3, pp. 1–24, Jul. 2017, doi: [10.1145/2983627](https://doi.org/10.1145/2983627).
- [19] H. Pang, J. Wang, A. Cao, and Q. Deng, "High-accuracy method for holographic image projection with suppressed speckle noise," *Opt. Exp.*, vol. 24, no. 20, p. 22766, Oct. 2016, doi: [10.1364/OE.24.022766](https://doi.org/10.1364/OE.24.022766).
- [20] J. Q. H. Nørgaard and T. L. Andersen, "Can the Rayleigh distribution be used to determine extreme wave heights in non-breaking swell conditions?" *Coastal Eng.*, vol. 111, pp. 50–59, May 2016, doi: [10.1016/j.coastaleng.2016.01.010](https://doi.org/10.1016/j.coastaleng.2016.01.010).
- [21] H. Lei, H. Zhang, I. S. Ansari, C. Gao, Y. Guo, G. Pan, and K. A. Qaraqe, "Performance analysis of physical layer security over generalized-K fading channels using a mixture gamma distribution," *IEEE Commun. Lett.*, vol. 20, no. 2, pp. 408–411, Feb. 2016, doi: [10.1109/LCOMM.2015.2504580](https://doi.org/10.1109/LCOMM.2015.2504580).
- [22] G. Zhang, J. Shi, and T. Zhang, "Stochastic resonance in a time-delayed tumor cell growth system driven by additive and multiplicative noises," *Modern Phys. Lett. B*, vol. 32, no. 22, pp. 1–11, 2018, doi: [10.1142/S0217984918502597](https://doi.org/10.1142/S0217984918502597).

- [23] C. You, W. Cong, M. W. Vannier, P. K. Saha, E. A. Hoffman, G. Wang, G. Li, Y. Zhang, X. Zhang, H. Shan, M. Li, S. Ju, Z. Zhao, and Z. Zhang, "CT super-resolution GAN constrained by the identical, residual, and cycle learning ensemble (GAN-CIRCLE)," *IEEE Trans. Med. Imag.*, vol. 39, no. 1, pp. 188–203, Jan. 2020, doi: [10.1109/TMI.2019.2922960](#).
- [24] W. Ji, J. Guo, and Y. Li, "Multi-head mutual-attention CycleGAN for unpaired image-to-image translation," *IET Image Process.*, vol. 14, no. 11, pp. 2395–2402, Sep. 2020, doi: [10.1049/iet-ipr.2019.1153](#).
- [25] F. Sheikholslami, D. Berberidis, and G. B. Giannakis, "Large-scale kernel-based feature extraction via low-rank subspace tracking on a budget," *IEEE Trans. Signal Process.*, vol. 66, no. 8, pp. 1967–1981, Apr. 2018, doi: [10.1109/TSP.2018.2802446](#).
- [26] Y. Chen, Y. Mai, J. Xiao, and L. Zhang, "Improving the antinoise ability of DNNs via a bio-inspired noise adaptive activation function rand softplus," *Neural Comput.*, vol. 31, no. 6, pp. 1215–1233, Jun. 2019, doi: [10.1162/neco\\_a\\_01192](#).
- [27] M. Zhao, M. Kang, B. Tang, and M. Pecht, "Deep residual networks with dynamically weighted wavelet coefficients for fault diagnosis of planetary gearboxes," *IEEE Trans. Ind. Electron.*, vol. 65, no. 5, pp. 4290–4300, May 2018, doi: [10.1109/TIE.2017.2762639](#).
- [28] Y. Li, N. Wang, J. Shi, X. Hou, and J. Liu, "Adaptive batch normalization for practical domain adaptation," *Pattern Recognit.*, vol. 80, pp. 109–117, Aug. 2018, doi: [10.1016/j.patcog.2018.03.005](#).
- [29] Z. Song, Y. Liu, R. Song, Z. Chen, J. Yang, C. Zhang, and Q. Jiang, "A sparsity-based stochastic pooling mechanism for deep convolutional neural networks," *Neural Netw.*, vol. 105, pp. 340–345, Sep. 2018, doi: [10.1016/j.neunet.2018.05.015](#).
- [30] Z. Zhao and X.-P. Zhou, "An integrated method for 3D reconstruction model of porous geomaterials through 2D CT images," *Comput. Geosci.*, vol. 123, pp. 83–94, Feb. 2019, doi: [10.1016/j.cageo.2018.11.012](#).
- [31] S. Jin, Y. Su, S. Gao, F. Wu, T. Hu, J. Liu, W. Li, D. Wang, S. Chen, Y. Jiang, S. Pang, and Q. Guo, "Deep learning: Individual maize segmentation from terrestrial lidar data using faster R-CNN and regional growth algorithms," *Frontiers Plant Sci.*, vol. 9, pp. 866–869, Jun. 2018, doi: [10.3389/fpls.2018.00866](#).
- [32] B. Cséfalvi, "Beyond trilinear interpolation: Higher quality for free," *ACM Trans. Graph.*, vol. 38, no. 4, pp. 1–8, Jul. 2019, doi: [10.1145/3306346.3323032](#).
- [33] G. Pizaine, E. D. Angelini, I. Bloch, and S. Makram-Ebeid, "Vessel geometry modeling and segmentation using convolution surfaces and an implicit medial axis," in *Proc. IEEE Int. Symp. Biomed. Imag., From Nano Macro*, Chicago, IL, USA, Mar. 2011, pp. 1421–1424, doi: [10.1109/ISBI.2011.5872666](#).
- [34] X. Chen, J.-N. Hwang, C.-N. Lee, and S.-I. Chen, "A near optimal QoE-driven power allocation scheme for scalable video transmissions over MIMO systems," *IEEE J. Sel. Topics Signal Process.*, vol. 9, no. 1, pp. 76–88, Feb. 2015, doi: [10.1109/JSTSP.2014.2336603](#).
- [35] K. H. Voo and D. B. Bong, "Quality assessment of stereoscopic image by 3D structural similarity," *Multimedia Tools Appl.*, vol. 77, no. 2, pp. 2313–2332, 2018, doi: [10.1007/s11042-017-4361-2](#).
- [36] K. Yu, L. Tan, X. Shang, J. Huang, G. Srivastava, and P. Chatterjee, "Efficient and privacy-preserving medical research support platform against COVID-19: A blockchain-based approach," *IEEE Consum. Electron. Mag.*, early access, Nov. 3, 2020, doi: [10.1109/MCE.2020.3035520](#).
- [37] Z. Zhou, Z. Wang, H. Yu, H. Liao, S. Mumtaz, L. Oliveira, and V. Frascolla, "Learning-based URLLC-aware task offloading for Internet of health things," *IEEE J. Sel. Areas Commun.*, vol. 39, no. 2, pp. 396–410, Feb. 2021, doi: [10.1109/JSAC.2020.3020680](#).



**JING ZHANG** was born in Xi'an, Shaanxi, China, in 1988. She received the B.S. degree from the Mathematics Department, Northwest University, Shaanxi, in 2010, the M.S. degree, in 2013, and the Ph.D. degree in computer science and technology from Northwest University, in 2018.

From 2018 to 2020, she was a Lecturer with the Xi'an University of Science and Technology, Shaanxi. She has been conducting one NSFC project and one project from the Shaanxi Science and Technology Department. She has been published ten articles in SCI and EI journal. Her research interests include image processing and 3D reconstruction techniques, fundamental study of signal processing, and signal imaging.



**DAN LI** was born in Baoji, Shaanxi, China, in 1997. She received the B.S. degree from the Software Engineering Department, Xi'an University of Science and Technology. She is currently pursuing the degree with the Department of Computer Science and Technology, Xi'an University of Science and Technology.

Her research interests include image processing and three-dimensional reconstruction technology.



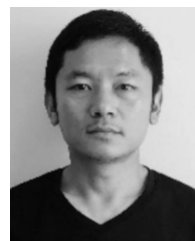
**QIAOZHI HUA** received the B.E. degree in electrical communication from the Wuhan University of Science and Technology, in 2011, and the M.S. and Ph.D. degrees from Waseda University, in 2015 and 2019, respectively. He is currently a Lecturer with the Computer School, Hubei University of Arts and Science, Hubei, China. His research interests include game theory and wireless communications.



**XIN QI** received the M.E. and Ph.D. degrees from Waseda University, Tokyo, Japan, in 2016 and 2019, respectively. He is currently a Research Associate with the Global Information and Telecommunication Institute, Waseda University. His research interests include ICN and 3N for next generation communication systems.



**ZHENG WEN** received the B.E. degree in computer science and technology from Wuhan University, China, in 2009, and the M.Sc. and Ph.D. degrees from Waseda University, Tokyo, Japan, in 2015 and 2019, respectively. He was a Research Associate with Waseda University, in 2018. He is currently an Assistant Professor (Lecturer) with the Department of Communication and Computer Engineering, Waseda University. His research interests include ICN/CCN for next-generation communication systems, AI, and the IoT.



**SAN HLAING MYINT** received the B.C.Tech., B.C.Tech. (Hons.), and M.C.Tech. degrees from the University of Computer Studies at Mandalay, Myanmar, in 2004, 2005, and 2008, respectively, and the Ph.D. degree from Waseda University, Tokyo, Japan, in 2019. From 2007 to 2015, he was a Tutor with the Ministry of Science and Technology, Myanmar. From 2009 to 2014, he was with the University of Computer Studies at Yangon, Myanmar, where he performed research focused on sustainable cloud computing. He is currently a Research Associate with the Global Information and Telecommunication Institute, Waseda University. His current research interests include fifth-generation wireless networks and analysis of channel coding methods.

...